Defense Technical Information Center
Compilation Part Notice

ADP012089

TITLE: Supercavitating 2-D Hydrofoils: Prediction of Performance and Design

DISTRIBUTION: Approved for public release, distribution unlimited

This paper is part of the following report:

TITLE: Supercavitating Flows [les Ecoulements supercavitants]

To order the complete compilation report, use: ADA400728

The component part is provided here to allow users access to individually authored sections of proceedings, annals, symposia, etc. However, the component should be considered within the context of the overall compilation report and not as a stand-alone technical report.

The following component part numbers comprise the compilation report:
ADP012072 thru ADP012091

SUPERCAVITATING 2-D HYDROFOILS: PREDICTION OF PERFORMANCE AND DESIGN

Spyros A. Kinnas

Ocean Engineering Group, Department of Civil Engineering
The University of Texas at Austin, Austin, TX 78712, USA
http://cavity.ce.utexas.edu, email: kinnas@mail.utexas.edu

ABSTRACT

Recent numerical techniques for the prediction of cavitating flows, in linear and non-linear theories, are applied on super-cavitating 2-D, 3-D hydrofoils and propellers. Some of these techniques, when incorporated within a non-linear optimization algorithm, can lead to efficient super-cavitating hydrofoil or propeller designs. This lecture will address 2-D supercavitating hydrofoils.

1   INTRODUCTION

High-speed hydrofoil or propeller applications can benefit considerably, in terms of efficiency, by operating under super-cavitating, ventilating, or surface-piercing conditions, as shown in Fig. 1. A photograph from a super-cavitating hydrofoil experiment that was performed at MIT's variable pressure Marine Hydrodynamics Water Tunnel is shown in Fig. 2. Photographs of a modern surface-piercing propeller when out and in the water are shown in Fig. 3.

Cavitating or free-streamline flows were first addressed in nonlinear theory via the hodograph technique as introduced by Helmholtz, Kirchoff and Levi-Civita (Birkhoff & Zarantonello 1957)[1]. The cavity surface in steady flow was taken as a steamline with constant pressure (thus, constant velocity). The first problems to be addressed involved flows around bluff bodies at zero cavitation number.

The formulation of the cavitating flow around bodies at non-zero cavitation numbers created a lot of diversity on the cavity termination models. Some of the first known models were the Riabouchinsky end-plate model and the re-entrant jet model. Open wake models were introduced in an attempt to model the viscous cavity wake (Fabula 1962, Tulin 1964, Yamaguchi & Kato 1983, Rowe & Blottiaux 1993, Kato 1994). Some of the existing cavity termination models were already covered in previous lectures in this course.

Due to the difficulty of the hodograph technique in dealing with general body shapes, very few cases have been treated analytically. The hodograph technique was extended numerically to treat arbitrary geometries (Wu & Wang 1964) and later applied to the analysis of super-cavitating hydrofoils in the presence of a free surface (Furuya 1975a). This method however, still could not treat general shape three dimensional geometries.

The linearized cavity theory was introduced by (Tulin 1953) and became quickly very popular, as proven by the vast amount of publications[2] which made use of it.

Unfortunately, the linearized theory for partially cavitating hydrofoils predicts that by increasing the thickness of a hydrofoil, the extent and size of the cavity, for constant flow conditions, also increases. This contradicts the fact that thicker hydrofoils have larger leading edge radii which are known to delay cavitation inception and therefore are expected to develop smaller cavities. In addition, it is well known that linear theory grossly overpredicts the cavity extent and volume, especially in the case of partial cavitation.

(Tulin & Hsu 1980) developed the short cavity theory by considering the cavitating flow as a small perturbation on the nonlinear fully wetted flow. Thus, the nonlinear foil thickness effects were included in this

---

[1]The list of references is located at the end of the second lecture of Prof. Kinnas.
[2]An extended list of which may be found in (Tulin & Hsu 1980) or (Kinnas 1991).
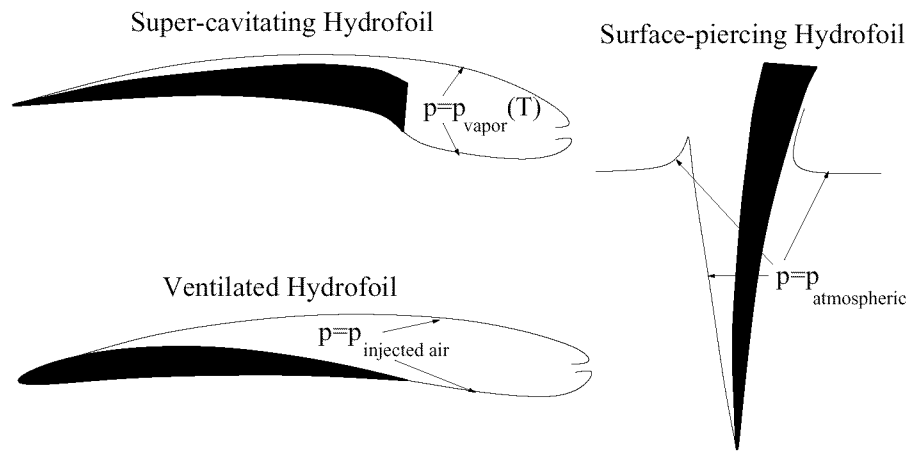
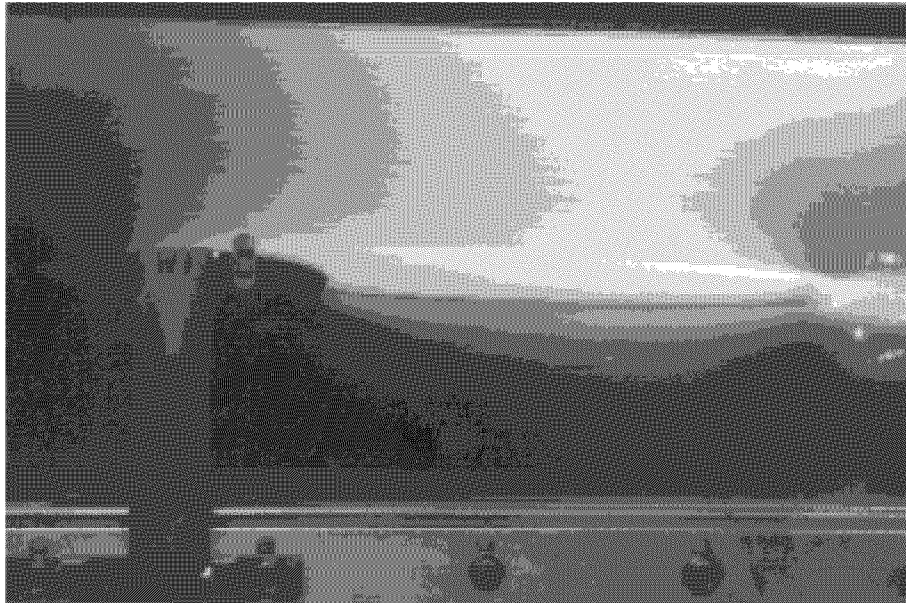Figure 1: Schematic of different types of high-speed hydrofoils.

Figure 2: Photo of a supercavitating hydrofoil experiment inside MIT's Marine Hydrodynamics Water Tunnel, $l/c \approx 3$, from Kinnas & Mazel, 1993.
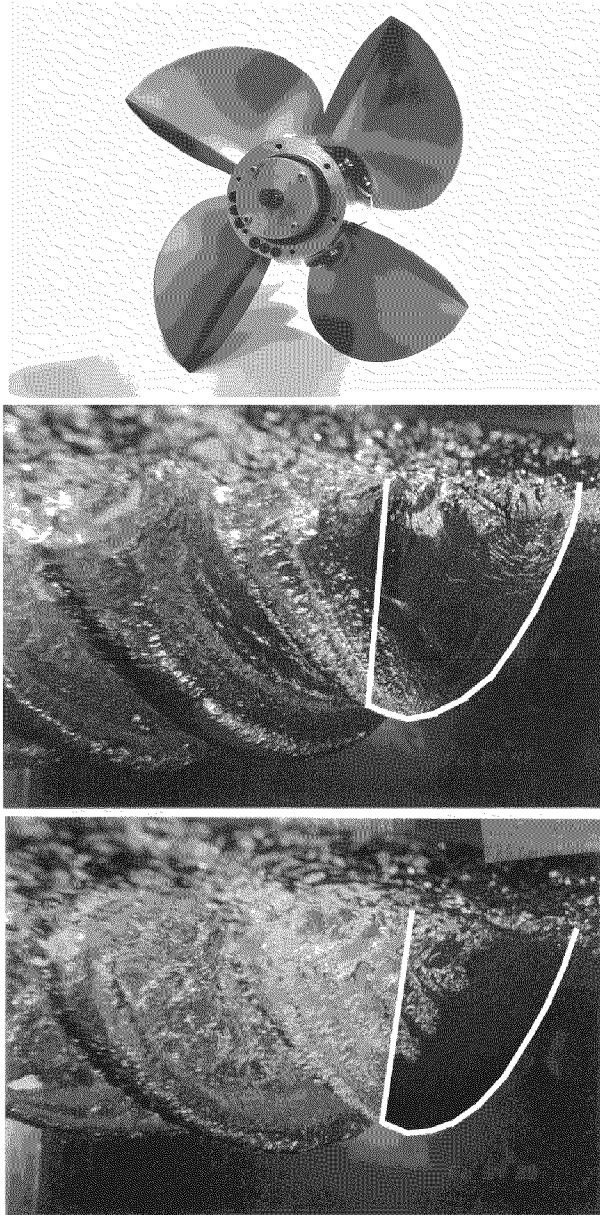
Figure 3: Photos of a surface-piercing propeller Model 841-B (top), and one of its blades after it has entered the free-surface, with leading edge detachment at $J_S = 0.9$ (middle), and with midchord detachment at $J_S = 1.0$ (bottom). For clarity, the blade has been outlined in the photos. From Olofsson (1996).

formulation. This method predicted that by increasing the thickness of a partially cavitating hydrofoil, the size of the cavity was reduced substantially for fixed flow conditions.

A nonlinear numerical method was employed to analyze cavitating hydrofoils by using surface vorticity techniques and by applying the exact boundary conditions on the cavity and on the foil (Uhlman 1987, Uhlman 1989). An end-plate cavity termination model was implemented. A reduction in the size of the cavity as the foil thickness increased was predicted, but not as drastic as that predicted in (Tulin & Hsu 1980). A surface vorticity technique to deal with thick foil sections which employed an open cavity model was developed in (Yamaguchi & Kato 1983). Similar boundary element method techniques were developed by (Lemonnier & Rowe 1988) and by (Rowe & Blottiaux 1993). Potential based boundary element methods were finally applied by (Kinnas & Fine 1991b, Kinnas & Fine 1993) and by (Lee et al 1992).

Three-dimensional flow effects around cavitating finite span hydrofoils were treated first in strip-theory via matching with an inner two-dimensional solution within either linear (Nishiyama 1970, Leehey 1971, Uhlman 1978, Van Houten 1982) or non-linear theory (Furuya 1975b).

The complete three-dimensional super-cavitating hydrofoil problem was first treated in linear theory via a numerical lifting surface approach based on the pressure source and doublet technique (Widnall 1966) and later via a vortex and source lattice technique (Jiang & Leehey 1977). In the latter work, an iterative scheme was introduced which determined the extent of the cavity by requiring the pressure distribution on the cavity to be constant along the span (in addition to being constant along the chord). A variational approach for determining the cavity planform was introduced in (Achkinadze & Fridman 1994).

Numerical boundary element methods within non-linear cavity theory were naturally extended to treat super-cavitating 3-D hydrofoils (Pellone & Rowe 1981) and 3-D hydrofoils with partial cavities (Kinnas & Fine 1993) or cavities with mixed (partial and super-cavities) planforms (Fine & Kinnas 1993a). Similar methods were also developed by (Kim et al 1994, Pellone & Peallat 1995).

The first effort to analyze the complete three dimensional unsteady flow around a cavitating propeller subject to a spatially non-uniform inflow was presented in (Lee 1979, Lee 1981, Breslin et al 1982). A source and vortex lattice lifting surface scheme was employed and the unsteady three dimensional *linearized* boundary conditions were applied on the cavity. The cavity planform was determined at each blade strip and each time step (i.e., blade angle) by searching for the cavity length which would produce the desired vapor pressure inside the cavity. The effect of the other strips was accounted for in an iterative sense by "sweeping" along the spanwise direction of the blade back and forth until the cavity shape converged. Similar methods were presented more recently by (Ishii 1992, Szantyr 1994, Kudo & Ukon 1994).

Unfortunately, all these 3-D methods are hampered by the inherent inability of linear cavity theory to predict the correct effect of blade thickness on cavity shape, as already mentioned. This deficiency was corrected in two dimensions in (Kinnas 1985, Kinnas 1991), where the *leading edge correction* was introduced in the linearized dynamic boundary condition on the cavity. The leading edge correction was subsequently applied to the three dimensional propeller solution (Kerwin et al 1986, Kinnas 1992b).

Non-linear methods based on an assumed semi-elliptic cavity sectional shape have also been applied (Stern & Vorus 1983) and (Van Gent 1994). Non-linear potential-based boundary element methods were finally applied to cavitating propellers in non-uniform flows by (Kinnas & Fine 1992, Fine & Kinnas 1993b), and more recently by (Kim & Lee 1996).

The inviscid cavity flow method was coupled with a boundary layer solver in the case of partial and super-cavitating 2-D hydrofoils by (Kinnas et al 1994). This allowed for the inclusion of the viscous boundary layer in the wake of the cavity and for determining the cavity detachment point based on the viscous flow upstream of the cavity.

Reynolds-Averaged Navier-Stokes solvers have also been applied in the case of the prediction of attached sheet cavitation on 2-D hydrodoils (Kubota et al 1989, Deshpande et al 1993). An overview of viscous flow solvers applied to cavitating flows may be found in (Kato 1996). However, these methods appear to be best suited for the prediction of cloud and or detached cavitation.

In these two lectures, linear and nonlinear methods for the prediction of super-cavitation on hydrofoils and propellers will be summarized, and some comparisons with experiments will be presented. Non-linear optimization techniques, applicable to the design of 2-D super-cavitating sections and super-cavitating propeller blades, will be also presented.
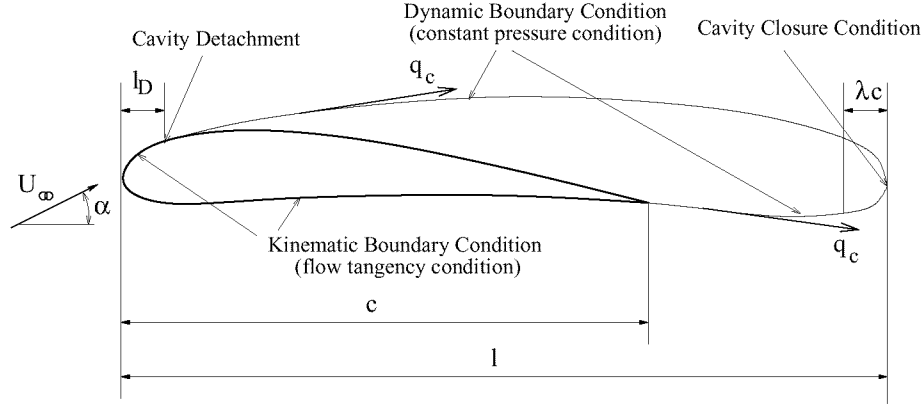
Figure 4: Formulation of the inviscid cavity flow problem

2 2-D HYDROFOIL

2.1 Formulation

Consider the 2-D super-cavitating hydrofoil[3], as shown in Fig. 4. Assuming inviscid and irrotational flow, the governing equation everywhere inside the fluid region is given by[4]:

$$\nabla^2 \phi = 0 \tag{1}$$

where ϕ is the the perturbation potential defined from:

$$\mathbf{q} = \mathbf{U}_\infty + \nabla \phi \tag{2}$$

where $\mathbf{q}$ is the total velocity vector in the flow. In order to uniquely determine ϕ, the following boundary conditions are imposed:

- On the wetted foil surface, the following kinematic boundary condition is applied, which requires the fluid flow to be tangent to the surface of the foil. Therefore,

$$\frac{\partial \phi}{\partial n} = -\mathbf{U}_\infty \cdot \mathbf{n} \tag{3}$$

where $\mathbf{n}$ is the surface unit normal vector.

- At infinity the perturbation velocities should go to zero.

$$\nabla \phi \to 0 \tag{4}$$

- The dynamic boundary condition specifies constant pressure on the cavity, or (via Bernoulli equation) constant cavity velocity q_c:

$$q_c = U_\infty \sqrt{1 + \sigma} \tag{5}$$

where the cavitation number, σ, is defined as:

$$\sigma = \frac{p_\infty - p_c}{\frac{\rho}{2} U_\infty^2} \tag{6}$$

p_∞ is the pressure corresponding to a point in the free-stream and p_c is the pressure inside the cavity.

---

[3]The application of the methods to partially cavitating hydrofoils is straight-forward and the reader can find more details in (Kinnas 1998).

[4]The cavity is assumed to detach at a known location on the foil. A criterion for determining this location will be discussed in a later section.
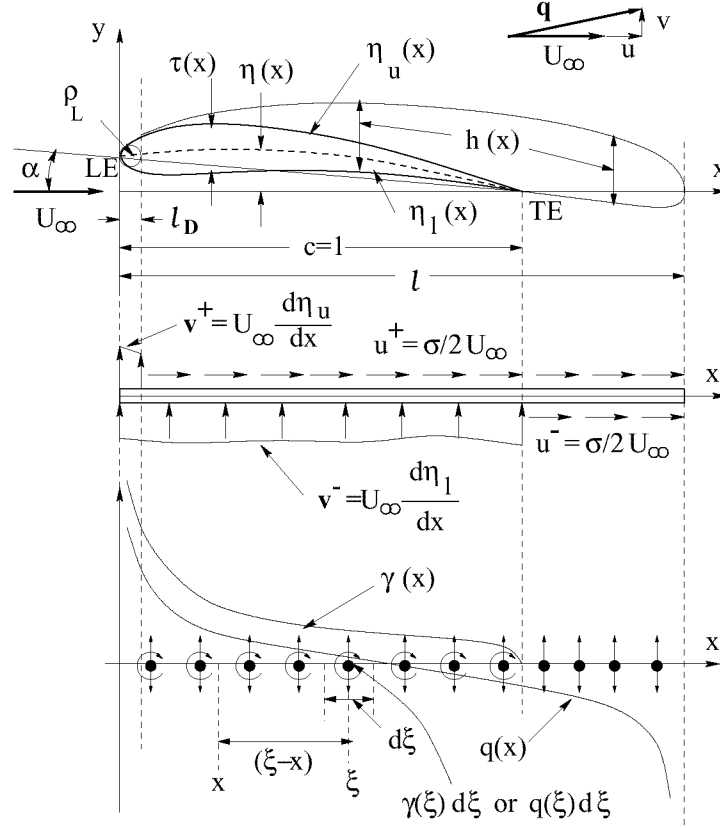
Figure 5: Supercavitating hydrofoil in linear theory.

- The following conditions at the trailing edge of the cavity:

  1. The cavity closes at its trailing edge. The inclusion of the viscous wake downstream of the cavity will be addressed in a later section.

  2. Near the trailing edge of the cavity, the pressure recovery termination model renders for the cavity velocity, q_{tr}, over a transition region λc:

$$q_{tr} = U_\infty \sqrt{1+\sigma}\,[1 - f(x)] \tag{7}$$

where $f(x)$ is an algebraic function defined in (Kinnas & Fine 1993).

The problem of finding the cavitation number for given cavity extent, l, will be addressed first in the context of linear and nonlinear theories. A method for determining the cavity extent for given cavitation number will be described in a later section.

2.2 Linear theories

In this section, the linearized cavitating hydrofoil problem is formulated in terms of singular integral equations with respect to unknown vorticity and source distributions. These integral equations are inverted analytically in the case of general shape supercavitating hydrofoils. The cavitation number, the vorticity and source distributions are expressed in terms of integrals of quantities which depend *only* on the foil geometry and the cavity length. The procedure is summarized here. The details are given in (Kinnas 1992a) and (Kinnas & Fine 1991a).

We define as u and v the perturbation velocities tangent and normal to the direction of the incoming flow respectively, as shown in Figure 5. In the context of the linearized cavity theory the boundary conditions of the corresponding Hilbert problem are:

The kinematic boundary conditions:

$$v^- = U_\infty \frac{d\eta_l}{dx} \; ; \;\; 0 < x < 1 \; , \; y = 0^- \tag{8}$$

$$v^+ = U_\infty \frac{d\eta_u}{dx} \; ; \;\; 0 < x < l_D \; , \; y = 0^+ \tag{9}$$

The dynamic boundary conditions:

$$u^+ \;\; = \;\; \frac{\sigma}{2} U_\infty \; ; \;\; l_D < x < l \; , \; y = 0^+ \tag{10}$$

$$u^- \;\; = \;\; \frac{\sigma}{2} U_\infty \; ; \;\; 1 < x < l \; , \; y = 0^- \tag{11}$$

where $\eta_l(x)$ and $\eta_u(x)$ are the ordinates of the lower and upper hydrofoil surface, respectively, as shown in Figure 5. These boundary conditions can be expressed in terms of vorticity and source distributions [5] $\gamma(x)$ and $q(x)$, respectively, located on the slit $x \in [0, l]$.

$$v^- \;\; = \;\; -\frac{q}{2} + \frac{1}{2\pi} \int_0^1 \frac{\gamma(\xi)d\xi}{\xi - x} \tag{12}$$

$$u^+ \;\; = \;\; \frac{\gamma}{2} - \frac{1}{2\pi} \int_0^l \frac{q(\xi)d\xi}{\xi - x} \tag{13}$$

$$u^- \;\; = \;\; -\frac{\gamma}{2} - \frac{1}{2\pi} \int_0^l \frac{q(\xi)d\xi}{\xi - x} \tag{14}$$

By using equations (10), (11), (13), and (14) it can easily be shown that:

$$\gamma(x) = 0; \;\; 1 < x < l \tag{15}$$

Finally, and with the use of the definitions:

$$\overline{\gamma}(x) = \frac{\gamma(x)}{\sigma U_\infty} \;\; \text{and} \;\; \overline{q}(x) = \frac{q(x)}{\sigma U_\infty} \; , \tag{16}$$

the complete boundary value problem becomes:

1. *Kinematic Boundary Conditions*

$$-\frac{\overline{q}}{2} + \frac{1}{2\pi} \int_0^1 \frac{\overline{\gamma}(\xi)d\xi}{\xi - x} = \Theta_l^*(x) \; ; \; 0 < x < 1 \; , \; y = 0^- \tag{17}$$

$$\frac{\overline{q}}{2} + \frac{1}{2\pi} \int_0^1 \frac{\overline{\gamma}(\xi)d\xi}{\xi - x} = \Theta_u^*(x) \; ; \; 0 < x < l_D \; , \; y = 0^+ \tag{18}$$

2. *Dynamic Boundary Condition*

$$\frac{\overline{\gamma}}{2} - \frac{1}{2\pi} \int_0^l \frac{\overline{q}(\xi)d\xi}{\xi - x} = \frac{1}{2} \; ; \; l_D < x < l \; , \; y = 0^+ \tag{19}$$

3. *Kutta Condition[6]*

$$\overline{\gamma}(1) = 0 \tag{20}$$

---

[5]With $\fint$ designating the Cauchy principal value of the integral.

[6]The application of a Kutta condition may seem unnecessary due to the requirement of a finite pressure, thus velocity, at the foil trailing edge. Nevertheless, this condition is still required when inverting the integral equations.

4. Cavity Closure Condition [7]

$$\int_0^l \overline{q}(x)dx = 0 \tag{21}$$

where

$$\Theta_l^* = \frac{1}{\sigma}\frac{d\eta_l}{dx} \quad \text{and} \quad \Theta_u^* = \frac{1}{\sigma}\frac{d\eta_u}{dx} \tag{22}$$

2.2.1 Inversion of the Integral Equations - $l_D = 0$

In the case of leading edge detachment ($l_D = 0$), the singular integral equations of Cauchy type, (17) and (19), can be inverted to produce expressions for the unknown σ, $\overline{\gamma}(x)$ and $\overline{q}(x)$ in terms of the cavity length l and the lower hydrofoil surface $\eta_l(x)$, as follows (Kinnas 1992a):

First, equation (19) is inverted with respect to the unknown $\overline{q}(x)$ (Muskhelishvili 1946) to produce:

$$\overline{q}(x) = -\sqrt{\frac{x}{l-x}} + \frac{1}{\pi}\sqrt{\frac{x}{l-x}}\int_0^1 \sqrt{\frac{l-\xi}{\xi}}\frac{\overline{\gamma}(\xi)d\xi}{x-\xi} \tag{23}$$

where use of equation (15) has been made. Notice that the expression (23) corresponds to the unique solution to (19) which behaves like $1/\sqrt{l-x}$ at the trailing edge of the cavity (Wu's singularity (Wu 1957)). By substituting equation (23) in (17) and by using the substitutions:

$$z = \sqrt{\frac{x}{l-x}}, \quad \eta = \sqrt{\frac{\xi}{l-\xi}}, \quad t = \sqrt{\frac{1}{l-1}}, \tag{24}$$

we arrive at the following singular integral equation of Cauchy type for $\overline{\gamma}$:

$$\frac{1}{2\pi}\int_0^t \frac{\overline{\gamma}(\eta)d\eta}{(1+\eta^2)(z-\eta)} = \frac{z}{4(1+z^2)} - \frac{\Theta_l^*(z)}{2(1+z^2)} \tag{25}$$

Inversion of equation (25) with respect to the variable $\overline{\gamma}(\eta)/(1+\eta^2)$ renders finally:

$$\overline{\gamma}(z) = -\frac{(1+z^2)}{\pi}\sqrt{\frac{t-z}{z}}\int_0^t \sqrt{\frac{\eta}{t-\eta}}\frac{\frac{\eta}{2} - \Theta_l^*(\eta)}{(1+\eta^2)(z-\eta)}d\eta \tag{26}$$

Notice that $\overline{\gamma}(z)$ in equation (26) is the unique solution to (25) which satisfies the Kutta condition (20) at $z = t$.

The cavitation number σ is determined by satisfying the cavity closure condition (21). First, by substituting equation (23) in (21) and by using equation (15) we can get (Kinnas 1992a):

$$-\frac{\pi l}{2} + \int_0^1 \sqrt{\frac{l-\xi}{\xi}}\overline{\gamma}(\xi)d\xi = 0, \tag{27}$$

and by substituting equation (26) we can get the following general expression for σ (Kinnas 1992a):

$$\sigma = \frac{4\sqrt{2}r^4}{\pi(r^2+1)}\int_0^t \sqrt{\frac{\eta}{t-\eta}}\frac{\sqrt{r^2+1}+\eta\sqrt{r^2-1}}{(1+\eta^2)^2}\left[-\frac{d\eta_l}{dx}\right]d\eta \tag{28}$$

where: $r = \sqrt{1+t^2}$.

The source distribution can be derived by substituting equation (26) into equation (23) (Kinnas 1992a):

$$\overline{q}(z) = -\Theta_l^*(z) + \sqrt{\frac{t+z}{z}}\frac{(\sqrt{r^2-1}-z\sqrt{r^2+1})}{2\sqrt{2}r^2} -$$
$$\frac{1+z^2}{\pi}\sqrt{\frac{t+z}{z}}\int_0^t \sqrt{\frac{\omega}{t-\omega}}\frac{\Theta_l^*(\omega)d\omega}{(1+\omega^2)(z+\omega)} \tag{29}$$

---

[7]We apply the linearized cavity closure condition in which the cavity is required to have zero thickness at its trailing edge. The present method can be extended to treat open cavities at the trailing edge with the openness of the cavity, possibly supplied from further knowledge of the viscous wake behind the cavity. The effects of viscosity will be addressed at a later section.

for $z < t$, and:

$$
\begin{aligned}
\overline{q}(z) \;=\; & \sqrt{\frac{t+z}{z}}\,\frac{(\sqrt{r^2-1}-z\sqrt{r^2+1})}{2\sqrt{2}r^2} - \\
& \frac{1+z^2}{\pi}\sqrt{\frac{t+z}{z}}\int_0^t \sqrt{\frac{\omega}{t-\omega}}\,\frac{\Theta_l^*(\omega)d\omega}{(1+\omega^2)(z+\omega)} - \\
& \sqrt{\frac{z-t}{z}}\,\frac{(z\sqrt{r^2+1}+\sqrt{r^2-1})}{2\sqrt{2}r^2} - \\
& \frac{1+z^2}{\pi}\sqrt{\frac{z-t}{z}}\int_0^t \sqrt{\frac{\omega}{t-\omega}}\,\frac{\Theta_l^*(\omega)d\omega}{(1+\omega^2)(z-\omega)}
\end{aligned}
\tag{30}
$$

for $z > t$.

2.2.2 Inversion of the Integral Equations - $l_D > 0$

In this case, as shown in (Kinnas & Fine 1991a), equations (26), (29), and (30) still apply, after the following substitutions are made:

$$
\text{replace}\ \ \overline{\gamma}\ \ \text{with}\ \ \overline{\gamma} - 2(u_{cw}^+ - \frac{1}{2})\ \ ;\ 0 < x < l_D
\tag{31}
$$

and

$$
\text{replace}\ \ \Theta_l^*\ \ \text{with}\ \ \Theta_l^* + F
\tag{32}
$$

with

$$
F(x) \stackrel{\text{def}}{=} -\frac{1}{\pi}\fint_0^{l_D} \frac{u_{cw}^+ - \frac{1}{2}}{\xi - x}\,d\xi
\tag{33}
$$

where u_{cw}^+ is the horizontal perturbation velocity on the wetted part on the suction side of the foil, divided by σU_∞. The value of u_{cw}^+ is determined by applying the kinematic boundary condition on the upper wetted part of the hydrofoil, equation (9). This is equivalent to requiring that the value of $q(x)$ for $0 < x < l_D$ is equal to the value of the thickness source in the case of wetted flow. A rather lengthy formula for u_{cw}^+, as well an expression for the modified value of σ are given in (Kinnas & Fine 1991a), and are not included in this lecture.

2.2.3 The cavity shape

The cavity thickness $h(x)$, which also includes the foil thickness as shown in Figure 5, is determined, within the framework of linearized theory, by integrating the equation:

$$
U_\infty \frac{dh}{dx} = q(x)
\tag{34}
$$

The camber of the cavity in the wake, $c(x)$, is determined by integrating the following equation:

$$
U_\infty \frac{dc}{dx} = v_w(x)\quad for\ \ 1 < x < l
\tag{35}
$$

where $v_w(x)$ is the normal perturbation velocity in the wake, given as follows:

$$
v_w(x) = -\frac{1}{2\pi}\int_0^1 \frac{\gamma(\xi)d\xi}{x-\xi}\ \ ;\ \ 1 < x < l,\ \ y = 0
\tag{36}
$$

By substituting equation (26) in (36) we can get v_w in terms of the hydrofoil geometry (Kinnas & Fine 1991a):

$$
\begin{aligned}
\frac{v_w(z)}{\sigma U_\infty} = {} & \sqrt{\frac{t+z}{z}}\,\frac{(\sqrt{r^2-1}-z\sqrt{r^2+1})}{4\sqrt{2}r^2} - \\
& \frac{1+z^2}{2\pi}\sqrt{\frac{t+z}{z}}\int_0^t \sqrt{\frac{\omega}{t-\omega}}\,\frac{\Theta_l^*(\omega)d\omega}{(1+\omega^2)(z+\omega)} - \\
& \sqrt{\frac{z-t}{z}}\,\frac{(z\sqrt{r^2+1}+\sqrt{r^2-1})}{4\sqrt{2}r^2} - \\
& \frac{1+z^2}{2\pi}\sqrt{\frac{z-t}{z}}\int_0^t \sqrt{\frac{\omega}{t-\omega}}\,\frac{\Theta_l^*(\omega)d\omega}{(1+\omega^2)(z-\omega)}
\end{aligned}
\tag{37}
$$

The pressure distribution on the upper and lower cavity or foil surface is given, in the context of linear theory, as follows:

$$
C_p^+ = -2\sigma\left[\frac{\overline{\gamma}}{2} - \frac{1}{2\pi}\int_0^l \frac{\overline{q}(\xi)d\xi}{\xi-x}\right] \quad ; \quad 0 < x < l \ , \ y = 0^+
\tag{38}
$$

$$
C_p^- = -2\sigma\left[-\frac{\overline{\gamma}}{2} - \frac{1}{2\pi}\int_0^l \frac{\overline{q}(\xi)d\xi}{\xi-x}\right] \quad ; \quad 0 < x < l \ , \ y = 0^-
\tag{39}
$$

where C_p is the pressure coefficient defined as:

$$
C_p = \frac{p-p_\infty}{\frac{\varrho}{2}U_\infty^2}
\tag{40}
$$

2.2.4 Numerical Integrations

The integrals in equations (28), (26), (29) and (30) are computed numerically with special care taken at the singularities of the integrands. We first define the transformation:

$$
\eta = t\,\sin^2\left(\frac{\theta}{2}\right) \quad ; \quad 0 \le \eta \le t \text{ and } 0 \le \theta \le \pi
\tag{41}
$$

Next, we expess the involved integrals in terms of θ, thus avoiding the square root singularities of the integrands at $\eta = 0$ and $\eta = t$. The numerical integrations are then performed by applying Simpson's rule with K uniform intervals in θ.

To compute the principal value of the singular integral in equation (26), we first factor out the involved singularity as follows (Kinnas 1992a):

$$
\int_0^t \sqrt{\frac{\eta}{t-\eta}}\,\frac{f(\eta)}{z-\eta}d\eta = \int_0^t \sqrt{\frac{\eta}{t-\eta}}\,\frac{f(\eta)-f(z)}{z-\eta}d\eta - \pi f(z)
\tag{42}
$$

where $f(\eta) = \frac{\frac{\eta}{2}-\Theta_l^*(\eta)}{1+\eta^2}$. Notice that the integrand in the integral of equation (42) is not singular anymore, and thus the integral is computed numerically by applying the same methodology described in the beginning of this section. As shown in (Kinnas 1992a), Simpson's rule produces very accurate values for the integrals even with five uniform intervals ($K = 5$).

2.2.5 The vortex/source-lattice method

A direct numerical method must be applied in the case of 3-D hydrofoils or propeller blades, as in (Lee 1979, Kinnas et al 1998a, Kosal 1999). In this case the involved integrals are disretized first, then the boundary conditions are applied at some appropriately selected control points (C.P.s), and finally, the resulting system of linear equations is inverted. The integrals in equations (17) and (19) are disretized over each segment i by replacing $\gamma(\xi)d\xi$ with $\gamma_i(X_{pv_{i+1}} - X_{pv_i})$, and $q(\xi)d\xi$ with $q_i(X_{ps_{i+1}} - X_{ps_i})$. Figure 6 shows two types of arrangements for the discrete vortices and sources and the correpsonding control points.
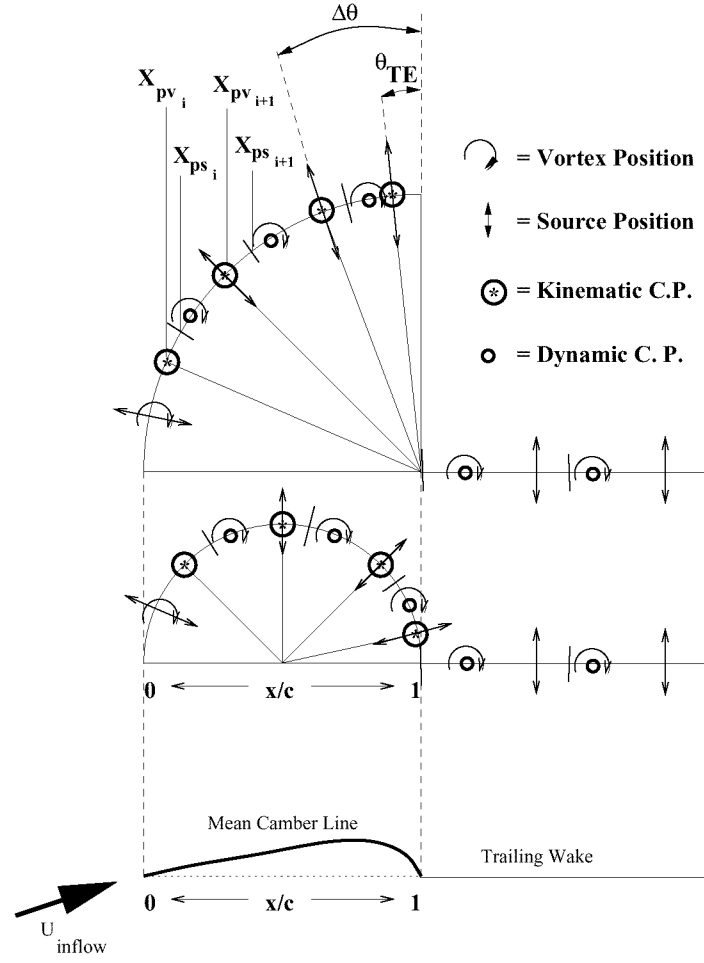
Figure 6: Half-cosine and full-cosine discretization scheme in the vortex/source-lattice method. The latter allows for a better representation of typical camber lines for super-cavitating hydrofoils.
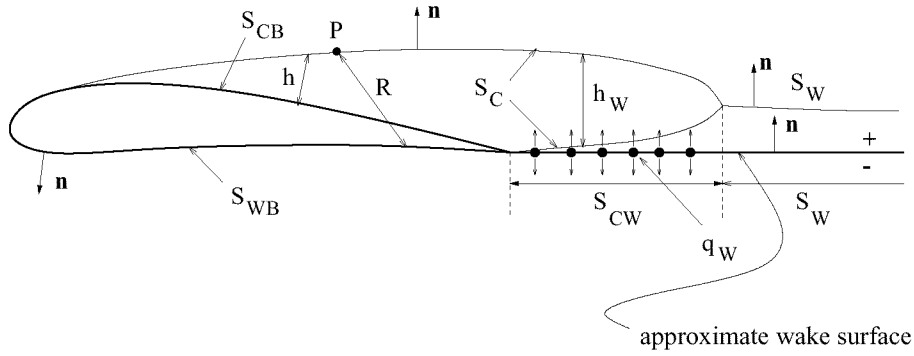

Figure 7: Super-cavitaitng non-linear theory. Definition of cavity, (wetted) body, and wake surfaces. The cavity sources in the wake are also shown in the case of the hybrid scheme.
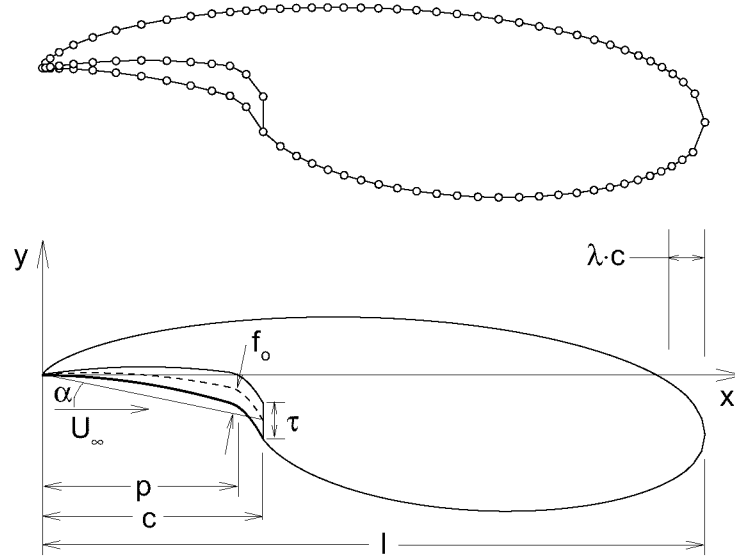
Figure 8: Super-cavitating hydrofoil. Definition of main parameters. Panel arrangement on the cavity and foil shown for $N = 80$.

2.3 Nonlinear theories

A potential based boundary element method which has applied has been applied for the analysis of cavitating hydrofoils in nonlinear cavity theory (Kinnas & Fine 1991b, Kinnas & Fine 1993, Fine & Kinnas 1993a), is summarized here, with emphasis on super-cavitating hydrofoils. The perturbation potential on the combined foil and cavity surface satisfies the following integral equation (Green's third identity):

$$\pi \phi_p = \int_{S_{WB} \cup S_C} \left[\frac{\partial \phi}{\partial n} \ln R - \phi \frac{\partial \ln R}{\partial n} \right] dS$$
$$- \int_{S_W} \Delta \phi_W \frac{\partial \ln R}{\partial n} dS \tag{43}$$

$\mathbf{n}$ is a unit vector normal to the foil or cavity surface, S_{WB} is the wetted body (foil) surface, S_C, the cavity surface, and S_W is the trailing wake surface, as shown in Fig. 7. R is the distance between a point, P, and the point of integration over the wetted foil, cavity, or wake surface, as shown in Fig. 7.

The foil and cavity surface are discretized into flat panels, as shown in Fig. 8. The source and dipole strengths are assumed constant over each panel. On the wetted foil surface, the source strengths, which are proportional to $\partial \phi / \partial n$, are given by the kinematic boundary condition, equation (3). On the cavity, the dipole strengths, which are proportional to ϕ, are determined from the application of the dynamic boundary condition (5) and (7). For simplicity $\lambda = 0$ for the rest of this paper; the complete derivation is given in (Kinnas & Fine 1993). It should be noted that the length of the transition region λ has been found to affect the results only locally. In the case of $\lambda = 0$ and when a large number of panels is used the formation of a re-entrant is observed(Krishnaswamy 1999).

$$q_c = \mathbf{U}_\infty \cdot \mathbf{s} + \frac{\partial \phi}{\partial s} = U_\infty \sqrt{1 + \sigma} \tag{44}$$

where s is the arclength along the cavity surface (measured from the cavity detachment point), and $\mathbf{s}$ is the unit vector tangent to the cavity surface. Integration of equation (44) renders the potential on the cavity surface:

$$\phi(s) = \phi(0) - \mathbf{U}_\infty \cdot \mathbf{s} + sU_\infty \sqrt{1 + \sigma} \tag{45}$$

Where $\phi(0)$ is the potential at the leading edge of the cavity. In the numerical scheme $\phi(0)$ is expressed in terms of the (unknown) potentials on the wetted part of the foil in front of the cavity.

The potential jump, $\Delta \phi_w$, in the wake is determined via the following condition:

$$\Delta\phi_w = \phi^+_{CTE} - \phi^-_{CTE} \tag{46}$$

where ϕ^+_{CTE} and ϕ^-_{CTE} are the potentials at the upper and lower cavity trailing edge panels, respectively. In two dimensions the effect of the trailing wake surface is equivalent to the effect of a concentrated vortex at the cavity trailing edge with strength equal to $\Delta\phi_w$.

The integral equation (43) is applied at the panel mid-points together with equations (46). The resulting linear system of equations is inverted in order to provide the unknowns: (a) ϕ on the wetted foil, (b) $\partial\phi/\partial n$ on the cavity, and (c) the corresponding cavitation number σ. The cavity shape is determined in an iterative manner. In the first iteration the panels representing the cavity are placed on the foil surface directly under the cavity. In subsequent iterations the cavity shape is updated by an amount $h(s)$ (applied normal to the cavity surface) which is determined from integrating the following ordinary differential equation[8]:

$$q_c\frac{dh}{ds} = \mathbf{U}_\infty \cdot \mathbf{n} + \frac{\partial\phi}{\partial n} \tag{47}$$

In addition, the cavity closure condition is enforced by the following equation:

$$h(s_L) = \frac{1}{q_c}\int\limits_0^{s_L}\left[\mathbf{U}_\infty \cdot \mathbf{n} + \frac{\partial\phi}{\partial n}\right]ds = 0 \tag{48}$$

s_L is the total arclength along the cavity surface.

The predicted cavity shapes and cavitation numbers have been found to converge quickly with number of iterations, especially in the case of super-cavitating hydrofoils.

This particular feature of the presented method makes it very attractive for 3-D and/or unsteady flow applications, where carrying more than one iterations would increase the computation time substantially. In fact the first iteration in the iterative scheme is determined by using the following *hybrid* scheme.

2.3.1 The hybrid scheme

In the case of 3-D hydrofoils and propeller blades, the following *hybrid* (combination of panel and source lattice method) scheme has been developed (Fine & Kinnas 1993a). In this scheme the panels representing the cavity are placed either on the foil surface underneath the cavity, S_{CB}, or on the approximate wake surface, S_{CW}, as shown in Fig. 7. Equation (43) then becomes(Fine & Kinnas 1993a):

$$
\begin{aligned}
\pi\phi_p &= \int_{S_B}\left[\frac{\partial\phi}{\partial n}\ln R - \phi\frac{\partial\ln R}{\partial n}\right]dS \\
&+ \int_{S_{CW}}q_W\ln R\,dS \quad - \int_{S_{CW}\cup S_W}\Delta\phi_W\frac{\partial\ln R}{\partial n}dS \\
&\qquad\qquad \text{for} \quad P \in S_B
\end{aligned} \tag{49}
$$

and

$$
\begin{aligned}
2\pi\phi^+_p = \pi\Delta\phi_W &+ \int_{S_B}\left[\frac{\partial\phi}{\partial n}\ln R - \phi\frac{\partial\ln R}{\partial n}\right]dS \\
&+ \int_{S_{CW}}q_W\ln R\,dS \quad - \int_{S_{CW}\cup S_W}\Delta\phi_W\frac{\partial\ln R}{\partial n}dS \\
&\qquad\qquad \text{for} \quad P \in S_{CW}
\end{aligned} \tag{50}
$$

where $S_B = S_{WB} \cup S_{CB}$ is the surface of the whole foil, and q_W is the cavity source in the wake surface given as:

$$q_W = \frac{\partial\phi^+}{\partial n} - \frac{\partial\phi^-}{\partial n} = q_c\frac{dh_W}{ds} \tag{51}$$

---

[8]As shown in (Kinnas & Fine 1993) this equation is equivalent to the kinematic boundary condition on the cavity surface.
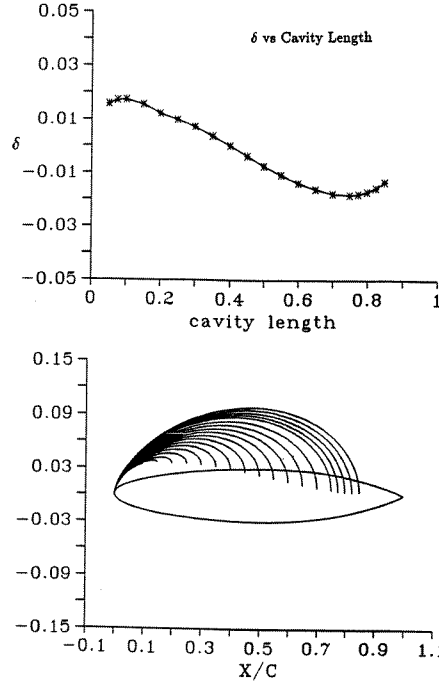
Figure 9: Predicted cavity trailing edge thickness and cavity shape for various cavity lengths at $\sigma = 1.097$ (corresponding to $l = 0.4$). From Kinnas and Fine, 1993.

where h_W is the cavity height measured normal to S_{CW}, as shown in Fig. 7. The cavity height h is measured normal to the foil surface for the part of the cavity that overlaps the foil, as also shown in Fig. 7.

The major advantage of the hybrid scheme is that it *can apply to all, wetted, partially, and super-cavitating flows alike* by utilizing the *same* panel discretization. In fact this scheme, as described in later sections, is applied on super-cavitating 3-D hydrofoils and propellers. In addition, this scheme has been found to predict the expected non-linear effect of foil thickness on the cavity shape in the case of partial cavitation (Kinnas & Fine 1993).

2.4 Cavity extent for given cavitation number

In the previous sections the cavity length was assumed to be known. In the case of linear theory, equation 28 can be inverted with respect to l for given σ. In the case of nonlinear theories the method can still be applied for the given σ and various "trial" cavity lengths. In this case though, due to the fact that the cavitation number is given (instead of being determined), the cavity closure condition, equation (48), or its equivalent $h_W(l) = 0$ in the case of the hybrid scheme, will not be satisfied.

$$\delta(l;\sigma) \equiv h_W(l) \neq 0 \tag{52}$$

This is shown for a partially cavitating hydrofoil in Fig. 9 where the predicted δ and the cavity shapes for fixed σ and different values of cavity length are shown. An iterative scheme has been developed (Kinnas & Fine 1993) for determining the cavity extent for given σ by searching for the cavity length, l, for which the cavity closes (within a specified tolerance) at its trailing edge[9]:

$$\delta(l;\sigma) = 0 \tag{53}$$

A comparison of predictions from applying the linear, the fully non-linear, and the hybrid cavity models to a super-cavitating hydrofoil is shown in Figure 10. All theories, including the conventional linear theory, appear

---

[9]An open cavity model can be readily implemented within this method by requiring the specified thickness at the cavity end.
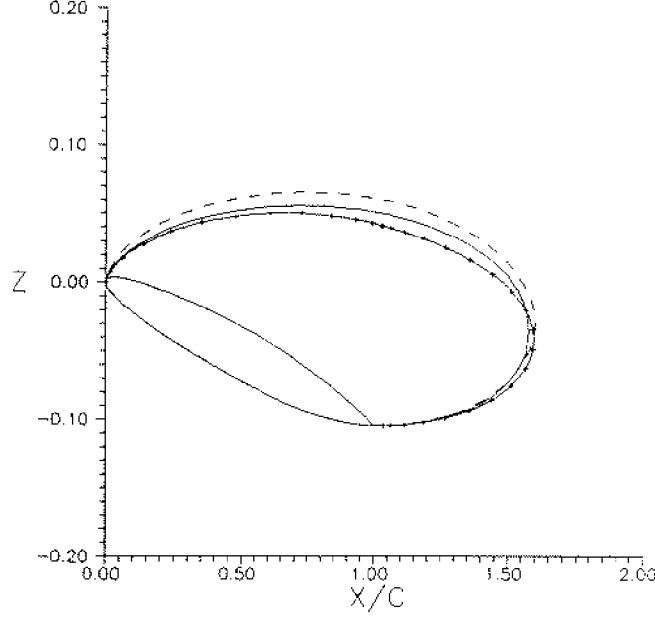
Figure 10: Comparison of predicted cavity shapes from linear (dashed), non-linear (solid) and hybrid (solid with dots) theories for NACA16004 at $\alpha = 6^o$. (dotted) linear; $\alpha/\sigma = 0.44$. From Fine and Kinnas (1993a).

to predict the cavity shape within satisfactory accuracy. Note that linear theory overpredicts the slope of the cavity at the leading edge.

Finally, a comparison of predicted versus measured velocity profiles in the vicinity of a 2-D supercavity is shown in Figure 11. In the prediction the wall effects have been included by using a sufficient number of multiple images with respect to the horizontal tunnel walls (Kinnas & Mazel 1992).

2.5 Effects of viscosity

Consider a super-cavitating hydrofoil in viscous flow, as shown in Figure 12. We first solve the inviscid cavity flow in non-linear theory (Kinnas & Fine 1991b). We then apply the boundary layer equations on the compound foil, confined by the pressure side of the hydrofoil and the cavity boundary. A zero friction condition is applied everywhere on the cavity, as shown in Figure 12. The effects of viscosity may be included by including the following term on the right-hand side of equation 43:

$$+ \int_{S_{WB} \cup S_C \cup S_W} \hat{\sigma} \ln R ds \qquad (54)$$

where the blowing sources, $\hat{\sigma}$, are defined from (Hufford et al 1994):

$$\hat{\sigma} = \frac{dU_e \delta^\star}{ds} \qquad (55)$$

where U_e is the edge velocity (in this case the same as the velocity predicted by the panel method when applied on the modified body that includes the displacement thickness) and $\delta^\star$ is the displacement thickess, which is determined from the boundary layer equations (Drela 1989).

Results from applying this method are shown in Figure 13. The resulting boundary layer displacement thickness is shown at the top of the figure. The pressure distributions in inviscid and viscous flow are also shown. Notice that viscosity has a very small effect on the pressure distribution. In other words, for super-cavitation, the cavitation number in viscous flow for given cavity length, l, is practically identical to that in inviscid flow. It should be noted that in the case of partial cavitation the effects of viscosity are much stronger than in the case of supercavitation (Kinnas et al 1994). The friction coefficient, C_f, on the pressure side of the foil and cavity, is also shown at the bottom part of Figure 13.

The lift and drag on the hydrofoil are evaluated by integrating the pressure forces acting on all sides of the hydrofoil (the constant cavity pressure is applied on the cavitating sides of the hydrofoil) as well as the frictional
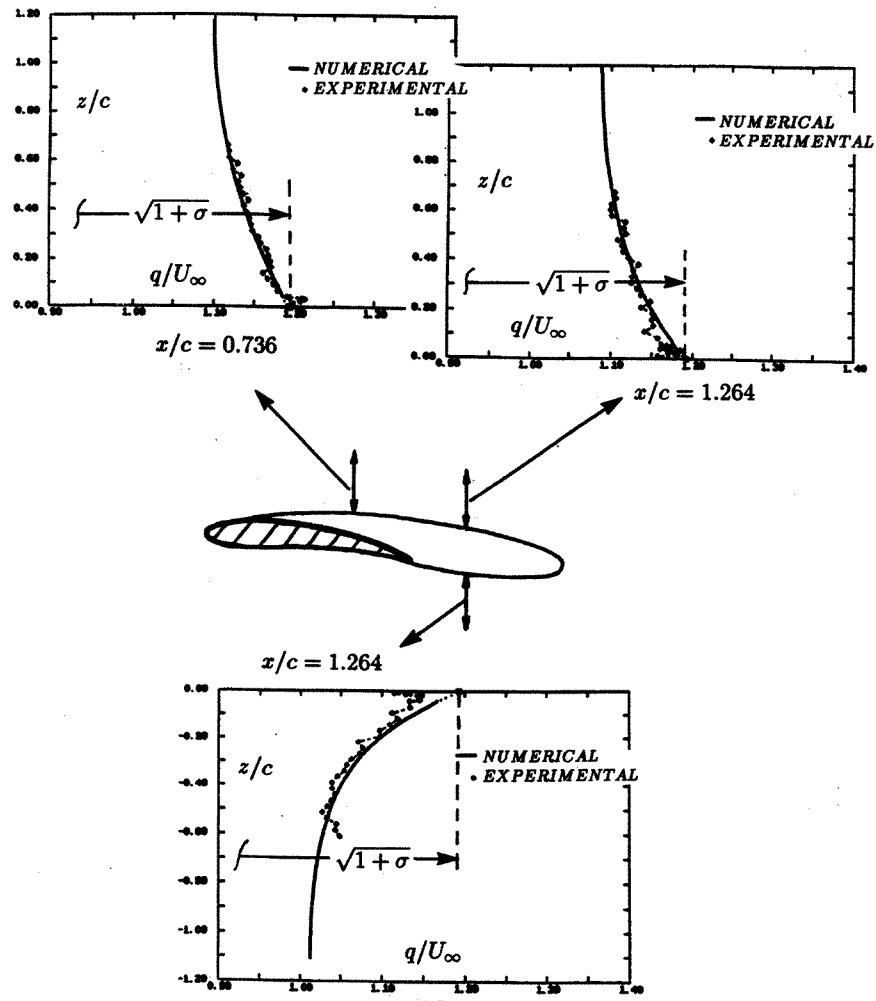
Figure 11: Numerical vs. experimental velocities as a function of the vertical distance from the cavity boundary at different chordwise locations. From Kinnas and Mazel (1993).
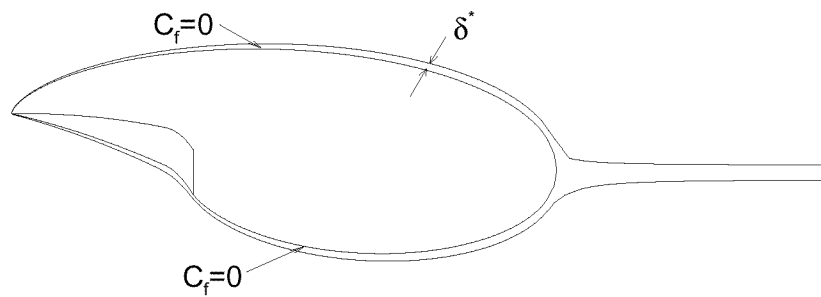

Figure 12: Super-cavitating hydrofoil with its boundary displacement thickness.
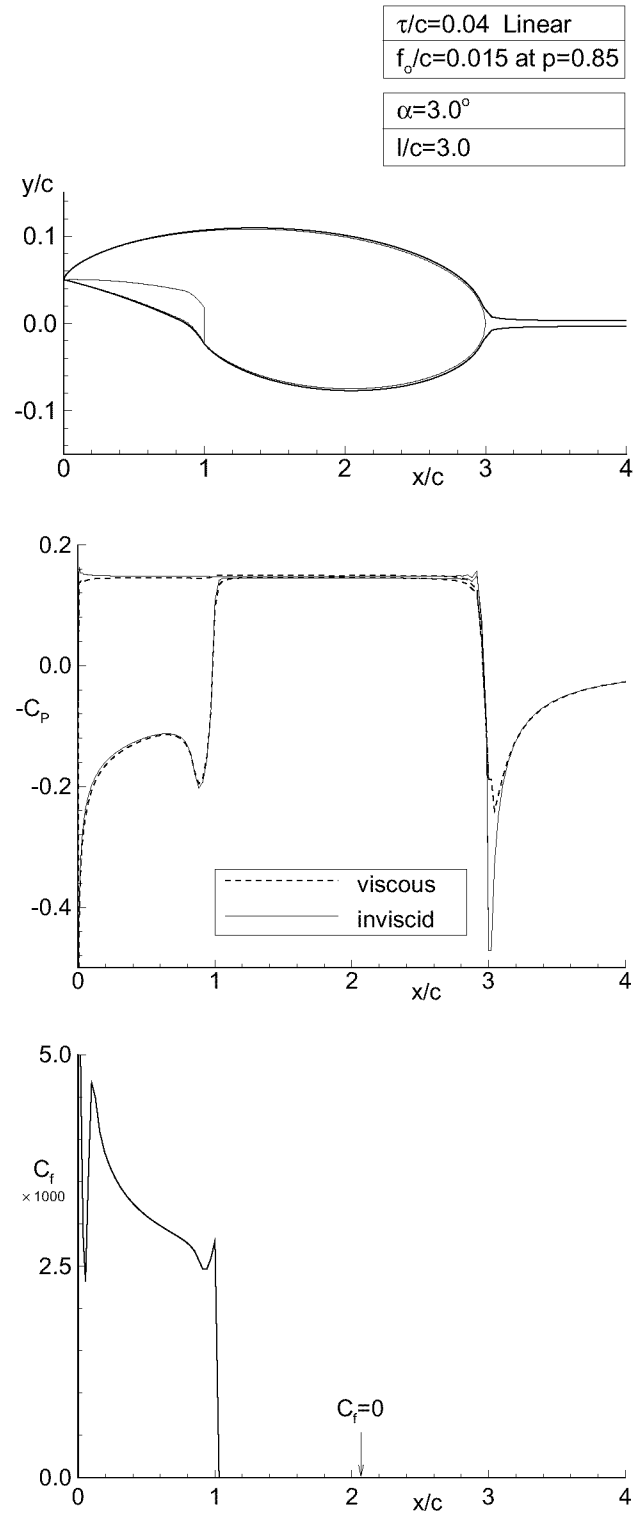
Figure 13: Super-cavitating hydrofoil in inviscid and viscous flow at $Re = 2 \times 10^7$. Cavity shape and boundary layer displacement thickness (top); pressure distributions (middle); and friction coefficient on the pressure side of the foil and cavity (bottom). All predicted by the present method.
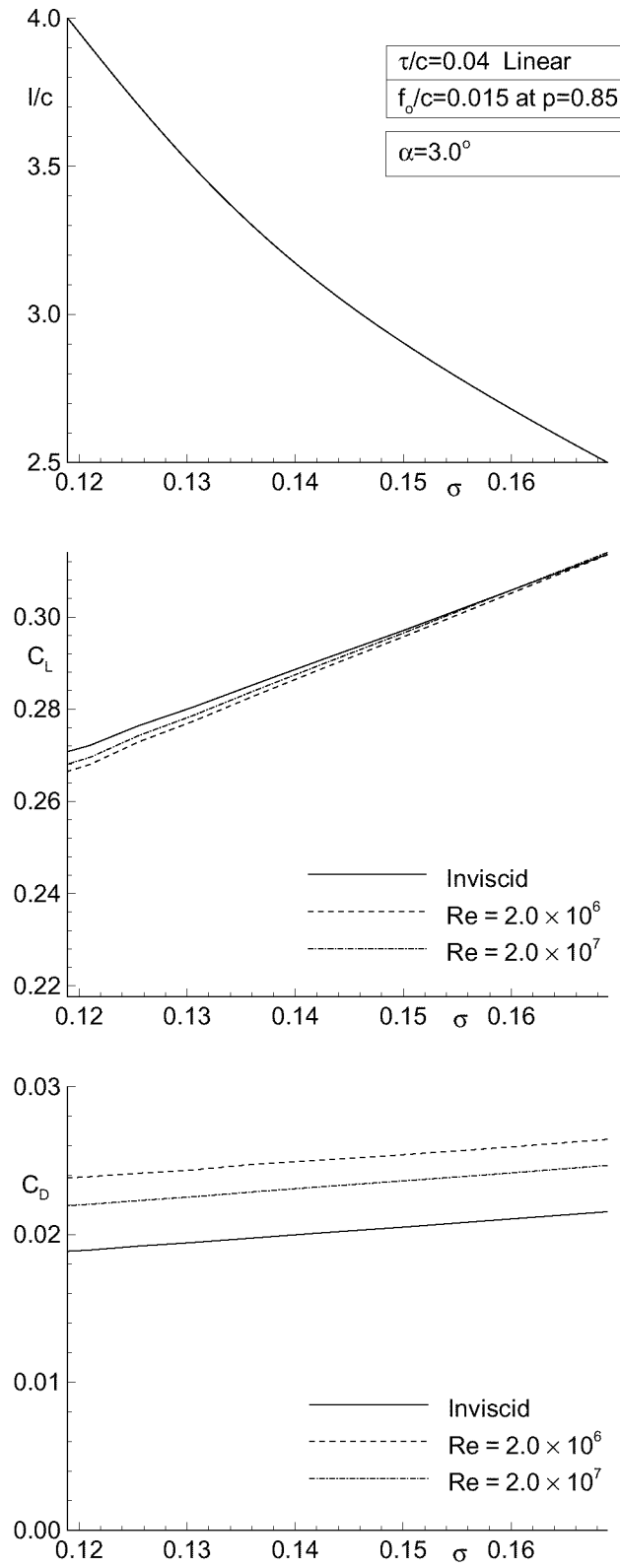
Figure 14: Cavity length, lift and drag coefficient versus cavitation number for a super-cavitating hydrofoil at $\alpha = 3^o$, in inviscid and viscous flow; predicted by the present method.

N	σ	V/c^2	C_L	C_D
100	0.145	0.365	0.282	0.0219
160	0.146	0.364	0.287	0.0223
200	0.146	0.363	0.292	0.0231

Table 1: Convergence of viscous cavity solution (σ, V/c^2, C_L and C_D) with number of panels. Super-cavitating hydrofoil; $\tau/c = 0.045$, $f_o/c = 0.015$, $p = 0.85$, $\alpha = 3^o$.
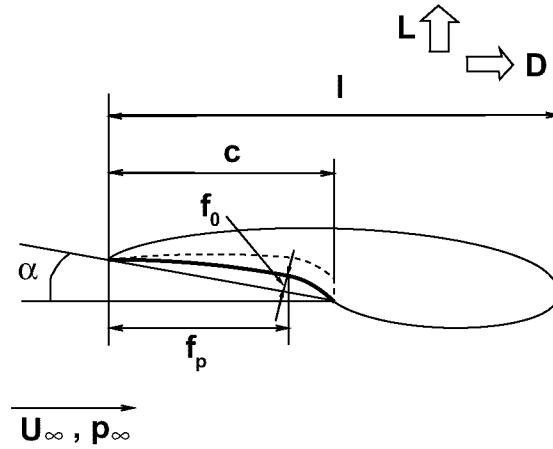

Figure 15: The main parameters in the design of a super-cavitating hydrofoil.

forces acting on the wetted side of the hydrofoil. The convergence of the cavity solution and the predicted forces with number of panels is given on Table 1.

Finally the predicted σ, C_L, and C_D vs. l curves are shown in Figure 14, for a super-cavitating section in inviscid flow and for two Reynolds numbers[10]. The super-cavitating section is a combination of a NACA 4digit camber form (with the maximum camber f_o at $x = p$) and a linear thickness form. The effect of viscosity on lift coefficient is shown to be very small.

3 DESIGN OF SURER-CAVITATING SECTIONS

3.1 Statement of the problem

We must determine the cavitating hydrofoil geometry and its operating condition (angle of attack, α), which produces the minimum drag, D, for specified design requirements.

The parameters that define the geometry of a super-cavitating hydrofoil, also shown in Figure 15, are:

- the chord, c

- the maximum camber, f_0, on the pressure side

- the location of the maximum camber, f_p

The design requirements taken into consideration in this paper are :

---

[10]Based on l.

- Sectional lift, $L_0 (N/m)$

- Uniform forward velocity of the foil, $U_\infty (m/s)$

- Cavitation number, σ_0, defined as usual:

$$\sigma_0 = \frac{p_\infty - p_v}{\frac{1}{2}\rho U_\infty^2} \tag{56}$$

where ρ is the fluid density, p_∞ is the ambient pressure, and p_v is the vapor pressure.

- Minimum section modulus of the foil, z_{min}

- Acceptable cavity length, l

- Acceptable cavity volume, V, or cavity height, h

The condition on the cavity length is necessary in order to avoid unstable cavities, usually being the long partial or the short super-cavities. The cavity volume/height constraints ensures acceptable positive cavity thickness (volume) in order to avoid very thin cavities (also negative thickness cavities) which are either non-physical or may turn into harmful bubble cavitation.

3.2   The hydrodynamic coefficients

The hydrofoil lift, L, and drag, D, acting on the hydrofoil, as shown in Figure 15, can be expressed in terms of lift and drag coefficients, C_L and C_D, respectively:

$$L = \frac{1}{2}\rho U_\infty^2 c C_L \tag{57}$$

$$D = \frac{1}{2}\rho U_\infty^2 c C_D \tag{58}$$

The drag coefficient, C_D, may be decomposed into two components.

$$C_D = C_D^i + C_D^v \tag{59}$$

where C_D^i is the inviscid cavity drag coefficient, and C_D^v is the viscous drag coefficient.

For known hydrofoil geometry, angle of attack, α, and cavity length, l, any hydrodynamic or cavity quantity, Q $(C_L, C_D^i, \sigma, V/c^2, ...)$, may be expressed as follows:

$$Q = Q(\alpha, \text{nondimensional foil geometry}, l/c) \tag{60}$$

Inviscid analysis methods are used to determine Q. The analytical formulas of (Hanaoka 1964) could have been used. These expressions though are based on linearized cavity theory, which has been found to overpredict the cavity length and size substantially, especially in the case of partial cavitation. Instead, in this work the already described numerical non-linear cavity analysis method is utilized (Kinnas & Fine 1991b, Kinnas & Fine 1993). The shape of the cavity surface is determined in non-linear theory iteratively, with the use of a low-order potential based panel method. The (inviscid) forces are determined by integrating the pressures along the foil surface.

The viscous drag is determined by assuming a uniform friction coefficient, C_f, over the wetted part of the foil. C_f is expressed in terms of the Reynolds number ($Re = U_\infty c/\nu$, ν : kinematic viscosity) via the ITTC formula (Comstock 1967):

$$C_f = \frac{0.075}{(log_{10}Re - 2)^2} \tag{61}$$

During the optimization process, the chord length (also the Reynolds number) is not known, thus the value of C_f is updated at each optimization iteration.

Since only the lower surface of the foil determines the hydrodynamics of supercavitating flows, the thickness is not included as a parameter. The upper surface can be placed anywhere arbitrarily inside the cavity. Thus, when computing the section modulus of a foil, the upper cavity surface is considered as the upper surface of the

"compound" foil. It is reasonable to assume that the cavity always starts at the leading edge of the foil, since the supercavitating sections have a sharp leading edge. Furthermore, we deal with situations where the cavity detaches at the trailing edge of the foil on the pressure side. For the case of supercavitating sections, in addition to specifying the minimum section modulus of the compound section, the minimum allowable cavity height at the 10% of the chord length from the leading edge is specified via an inequality constraint. This ensures positive cavity thickness, as well as sufficient local strength at the sharp leading edge of the foil.

The relevant coefficients are expressed as follows:

$$
\begin{aligned}
C_L &= C_L(\alpha, f_0/c, f_p/c, l/c) \\
C_D^i &= C_D^i(\alpha, f_0/c, f_p/c, l/c) \\
\sigma &= \sigma(\alpha, f_0/c, f_p/c, l/c) \\
V/c^2 &= V/c^2(\alpha, f_0/c, f_p/c, l/c) \\
z/c^3 &= z/c^3(\alpha, f_0/c, f_p/c, l/c) \\
h_{10}/c &= h_{10}/c(\alpha, f_0/c, f_p/c, l/c)
\end{aligned}
$$

where h_{10} is the cavity height at the 10% of the chord length from the leading edge of the foil. Note that the section modulus is a function of all the geometry variables including the cavity length, whereas it is independent of the cavity length in the case of partial cavitation.

The coefficients are computed, as in the case of partial cavitation, for a number of foil geometries by using the analysis method of (Fine & Kinnas 1993a). The coefficients are again expressed by using second degree polynomials in terms of all the geometric parameters. For example,

$$
C_L = C_{L_1}\alpha + C_{L_2}\alpha^2 + C_{L_3}\frac{f_0}{c} + C_{L_4}\left(\frac{f_0}{c}\right)^2
$$

$$
+ C_{L_5}\frac{f_p}{c} + C_{L_6}\left(\frac{f_p}{c}\right)^2 + C_{L_7}\frac{l'}{c} + C_{L_8}\left(\frac{l'}{c}\right)^2
$$

$$
+ C_{L_9}\alpha\frac{f_0}{c} + C_{L_{10}}\alpha\frac{f_p}{c} + C_{L_{11}}\alpha\frac{l'}{c} + C_{L_{12}}\frac{f_0}{c}\frac{f_p}{c}
$$

$$
+ C_{L_{13}}\frac{f_0}{c}\frac{l'}{c} + C_{L_{14}}\frac{f_p}{c}\frac{l'}{c} + C_{L_{15}} \tag{62}
$$

where,

$$
\frac{l'}{c} = \frac{1}{\sqrt{1 - (c/l)^2} + 1 - (c/l)^2} \tag{63}
$$

The variable transformation from l/c to l'/c is done knowing that C_L and C_D are linear in l'/c for the super-cavitating flat plate in linear theory, as described by (Geurst 1960). This transformation has been found to improve the accuracy of the interpolation substantially. The effect of the number of The accuracy of the interpolation for C_D may be seen in Figures 16.

3.3 The optimization problem

Consider the following general nonlinear optimization problem:

$$
\begin{aligned}
\text{minimize} \quad & f(\mathbf{x}) \\
\text{subject to} \quad & g_i(\mathbf{x}) \leq 0 \quad i = 1, 2, \ldots, m \\
& h_i(\mathbf{x}) = 0 \quad i = 1, 2, \ldots, l
\end{aligned} \tag{64}
$$

where $f(\mathbf{x})$ is the objective function defined on $\mathcal{R}^n$. $\mathbf{x}$ is the solution vector of n components. $g_1(\mathbf{x}) \leq 0, \ldots, g_m(\mathbf{x}) \leq 0$ are inequality constraints defined on $\mathcal{R}^n$ and $h_1(\mathbf{x}) = 0, \ldots, h_l(\mathbf{x}) = 0$ are equality constraints also defined on $\mathcal{R}^n$.

The solution vector is defined as ($n = 5$):

$$
\mathbf{x} = [\alpha, c, f_0, f_p, l]^T \tag{65}
$$

The constraints are ($m = 3, l = 2$)

$$h_1(\mathbf{x}) = L(\mathbf{x}) - L_0 = 0 \tag{66}$$

$$h_2(\mathbf{x}) = \sigma(\mathbf{x}) - \sigma_0 = 0 \tag{67}$$

$$g_1(\mathbf{x}) = -\frac{l}{c} + \left(\frac{l}{c}\right)_{min} \leq 0 \tag{68}$$

$$g_2(\mathbf{x}) = -\frac{z(\mathbf{x})}{c^3} + \frac{z_{min}}{c^3} \leq 0 \tag{69}$$

$$g_3(\mathbf{x}) = -\frac{h_{10}(\mathbf{x})}{c} + \left(\frac{h_{10}}{c}\right)_{min} \leq 0 \tag{70}$$

3.4 The numerical optimization method

The method of multipliers is applied in which, first each of the inequality contraints, $g_i(\mathbf{x}) \leq 0$, is converted into an equality constraint with the introduction of the new variable, s_i:

$$g_i(\mathbf{x}) + s_i^2 = 0 \tag{71}$$

Then the augmented Langrangian penalty function is formed (Mishima & Kinnas 1996):

$$F(x_1, ..., s_1, ..., \lambda_1, ..., \tilde{\lambda}_1, ..., c_1, ..., \tilde{c}_1, ...) =$$
$$D(\mathbf{x}) + \Sigma \lambda_i h_i(\mathbf{x}) + \Sigma \tilde{\lambda}_i [g_i(\mathbf{x}) + s_i^2]$$
$$+ \Sigma c_i h_i^2(\mathbf{x}) + \Sigma \tilde{c}_i [g_i(\mathbf{x}) + s_i^2]^2 \tag{72}$$

where λ_i and $\tilde{\lambda}_i$ are the Langrange multipliers, and c_i and $\tilde{c}_i$ are penalty parameters. The parameters of the problem, the additional parameters (s_i), the Langrange multipliers, and the penalty parameters are determined by minimizing function F. A technique to minimize F is described in great detail in (Mishima & Kinnas 1996).

3.5 Effect of the initial guess on the optimum solution

In general, a nonlinear optimization problem is initial guess dependent. In other words, if there exist more than one local minimum to the objective function, any one of these minima may be obtained depending on the initial condition. Due to the special structure of the problem, no multiple solutions were found for the range of cavitation numbers that we studied. This uniqueness is attributed partly to the fact that the involved functions are quadratic, i.e. not wavy, and partly to the fact that the range of the solutions is known, so that a reasonable initial guess can be selected. Figure 17 shows that several different initial guesses lead to the same solution.

3.6 Results

A NACA 4 digit camber form and the Johnson five-term camber form are used. The NACA 4digit camber form (Abbott & Von Doenhoff 1959) has two parameters, which are the maximum camber f_0/c and the location of the maximum camber f_p/c, as shown in Figure 15. The values for the constraints are:

$$\left(\frac{l}{c}\right)_{min} = 1.15 \quad \left(\frac{h_{10}}{c}\right)_{min} = 0.01 \quad \left(\frac{z_{min}}{c^3}\right) = 7 \times 10^{-5} \tag{73}$$

The method is applied for fixed lift ($L_0 = 30,000 N/m$) and for a range of cavitation numbers between 0.15 and 0.7 (corresponding to approximate speeds of 70 and 30 knots, respectively[11]) for partial and super-cavitating conditions. The resulting L/D for both cases are shown in Figure 18. As expected, for "low" σ a supercavitating section has larger L/D than a partially cavitating section, and the reverse holds for larger σ. Optimum partially and supercavitating sections are also shown in Figure 18.

Finally, we show in Figure 19, contour plots of L/D for optimum sections, designed by the present method, over a range of combinations of required lift and cavitation number. This graph is intended to help the designer decide as to what is the best solution (partially or supercavitating section), depending on the requirements.

---

[11]The cavitation number is inversely proportional to the square of the speed of the hydrofoil, for fixed ambient pressure and temperature conditions.

3.7 Comparison of the present to existing design methods

The designed sections, under given requirements, are compared to those designed from other methods. These methods are based on either the Tulin two-term or the Johnson five-term sections, given next:

$$\frac{y}{c} = \frac{A_1}{2}\left\{\frac{x}{c} + \frac{8}{3}\left(\frac{x}{c}\right)^{3/2} - 4\left(\frac{x}{c}\right)^2\right\} \quad \text{(Tulin two-term)} \tag{74}$$

$$\frac{y}{c} = \frac{A_1}{315}[210\left(\frac{x}{c}\right) - 2240\left(\frac{x}{c}\right)^{3/2} + 12600\left(\frac{x}{c}\right)^2$$
$$- 30912\left(\frac{x}{c}\right)^{5/2} + 35840\left(\frac{x}{c}\right)^3 - 15360\left(\frac{x}{c}\right)^{7/2}]$$
$$\text{(Johnson five-term)} \tag{75}$$

where A_1 is a parameter that relates the geometry to the lift coefficient.

As the number of terms included in the series increases, the loading moves towards the trailing edge. A useful formula for the finite cavitation number correction is given by (Ohba 1963/1964) as follows.

$$C_L = \sqrt{C_{L,\sigma=0}^2 + 0.85\sigma^2} + \sigma C_{L,\sigma=0} \tag{76}$$

where C_L is the required lift coefficient and $C_{L,\sigma=0}$ is the lift coefficient for zero cavitation number.

In Figure 20, the lift to drag ratio, L/D, is shown for the NACA 4dgt sections designed by the present method, Tulin's two-term sections, and Johnson's five-term sections, for various cavitation numbers. In the same figure we also show the L/D for the optimum Johnson section as designed by the present method. The corresponding lift coefficients are shown in Figure 21. For the design of Tulin sections and Johnson sections, the cavitation number and the lift coefficient are both specified, whereas in the present method, the cavitation number and the lift are given and the lift coefficient is determined as part of the solution. A representative section and its corresponding pressure distribution is shown in Figure 22.

3.8 Application to 3-D elliptic planform hydrofoils

As shown in (Kinnas et al 1995), a super-cavitating hydrofoil with elliptic planform and similar sections along its span (that are only scaled by the chord), can be designed by designing an equivalent 2-D section. If c and s_o are the maximum chord and span of the elliptic wing, the equivalent 2-D lift is given from:

$$L_{2D} = L_{3D}\frac{4}{\pi s_o} \tag{77}$$

If D_{2D} is the corresponding minimum value of the drag then D_{3D} will be given as:

$$D_{3D} = \frac{L_{3D}^2}{1/2\rho U_\infty^2 \pi s_o^2} + \frac{\pi s_o}{4}D_{2D} \tag{78}$$

The above equation can be re-written as:

$$\frac{D_{3D}}{L_{3D}} = \frac{L_{3D}}{1/2\rho U_\infty^2 \pi s_o^2} + \frac{D_{2D}}{L_{2D}} \tag{79}$$

Equation (79) implies that $(L/D)_{3D}$ will always be smaller than $(L/D)_{2D}$, i.e. the 3-D hydrofoil will always be *less* efficient than the 2-D hydrofoil.

The actual angle of attack α_{3D} will be related to that determined from the 2-D equivalent optimization problem as:

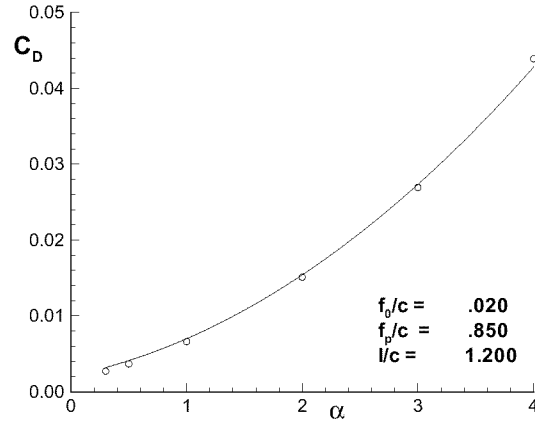$$\alpha_{3D} = \alpha_{2D} + \frac{L_{3D}}{1/2\rho U_\infty^2 \pi s_o^2} \tag{80}$$

Figure 16: Accuracy of the interpolation : Supercavitation (C_D vs α), Range of parameters: $\alpha = 0.3 \sim 4.0$ deg (6 points), $f_0/c = 0.0 \sim 0.05$ (6 points), $f_p/c = 0.7 \sim 0.9$ (5 points), $l/c = 1.1 \sim 1.3$ (4 points)
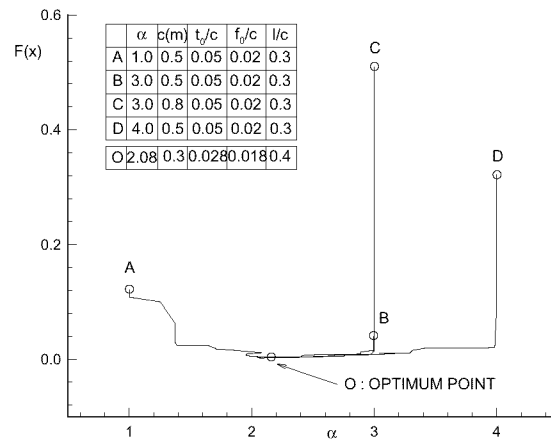

Figure 17: Sensitivity of the optimum solution on initial guesses , $L = 30,000(N/m), \sigma = 0.6, U_\infty = 18.2(m/s)$
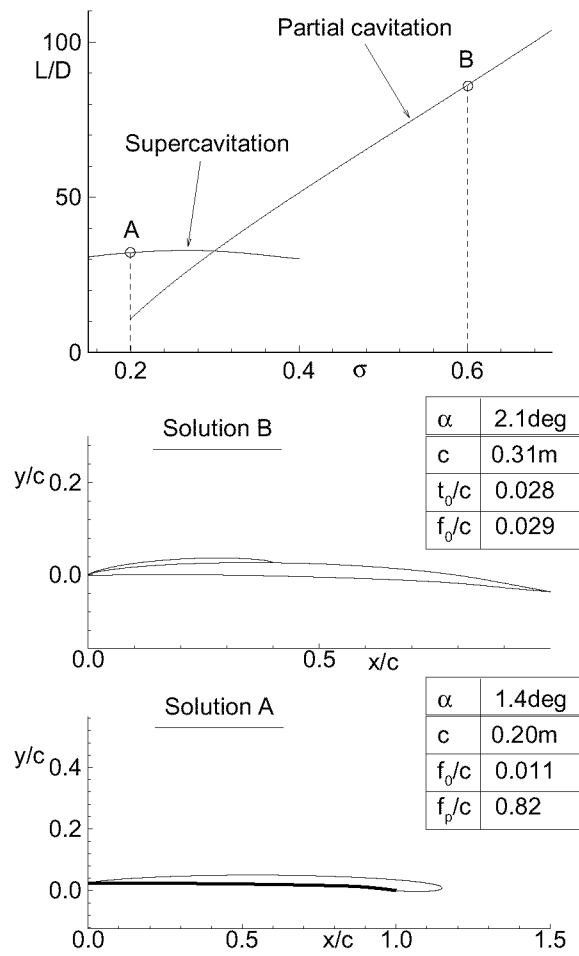
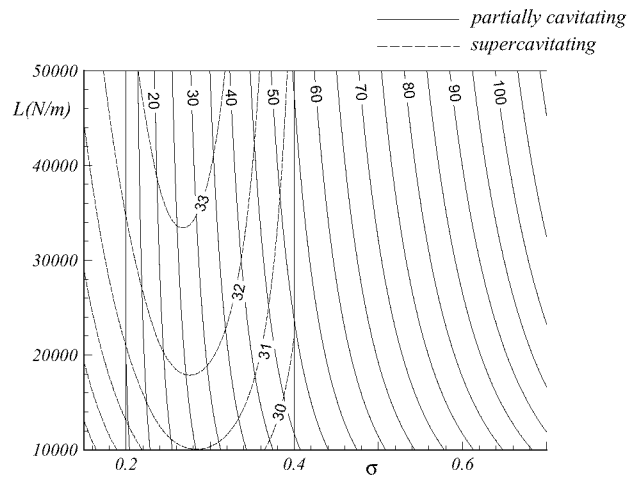Figure 18: L/D for partially or super-cavitating foils designed by the present method; $L_0 = 30,000N/m$.

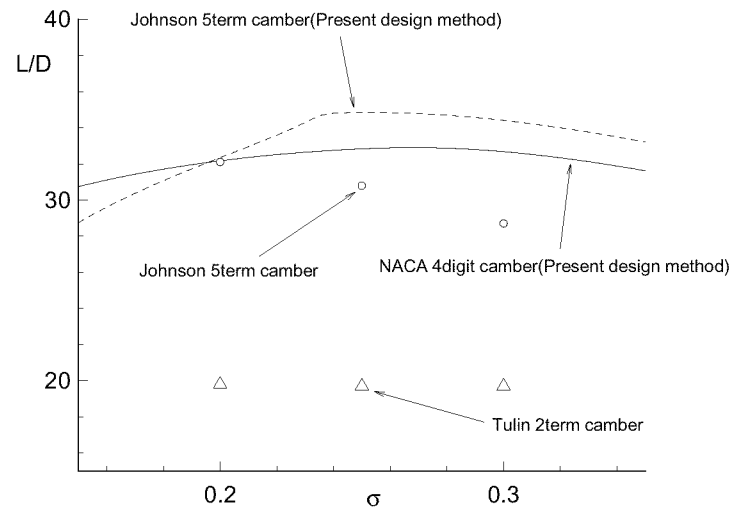Figure 19: Contour plots of L/D for partially or super-cavitating foils designed by the present method.

Figure 20: Comparison of L/D between designed sections and existing sections ($L = 30000(N/m), z_{min}/c^3 = 7.0 \times 10^{-5}$ (supercavitating)
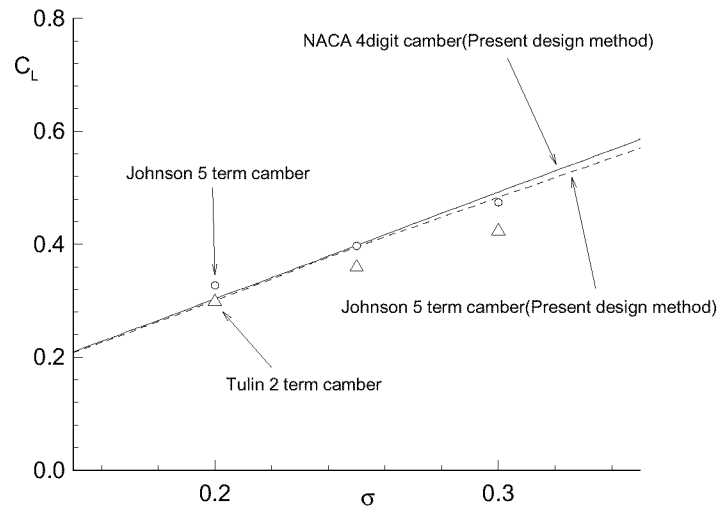

Figure 21: Comparison of C_L between designed sections and existing sections ($L = 30000(N/m), z_{min}/c^3 = 7.0 \times 10^{-5}$ (supercavitating)
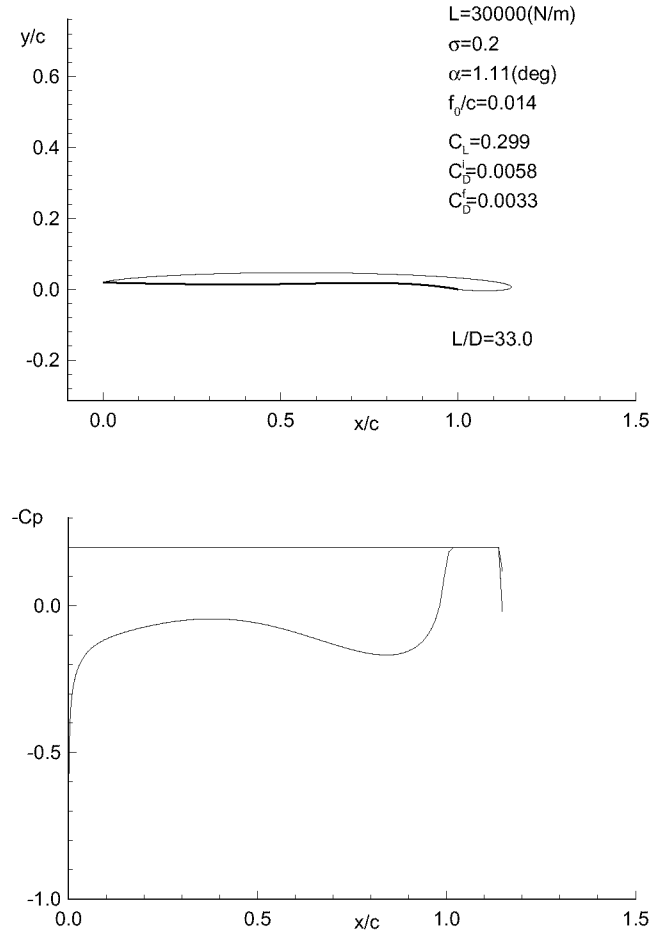
Figure 22: Optimum supercavitating section and corresponding pressure distribution; designed by the present method (Johnson five-term camber : $L = 30000(N/m), \sigma = 0.2, z_{min}/c^3 = 7.0 \times 10^{-5}$)